RSC Advances




ROYAL SOCIETY OF CHEMISTRY

www.rsc.org/advances

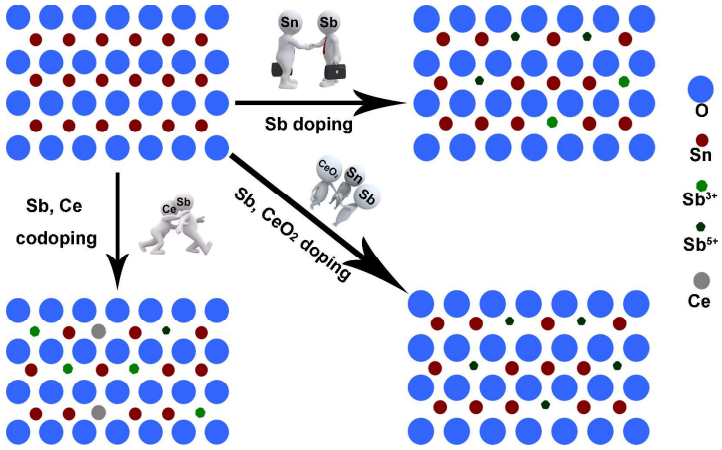


Nano-$CeO_2$ doping mitigates the surface antimony enrichment and promotes the complete oxidation of antimony, while cerium ion doping aggravates that.

# Different Mechanism and Electrocatalytic Activity of Ce ion or $CeO_2$ Modifying Ti/Sb-$SnO_2$ Electrode fabricated by One-step Pulse Electro-codeposition

Tigang Duan, Ye Chen*, Qing Wen*, Ying Duan

*Key Laboratory of Superlight Materials and Surface Technology of Ministry of Education, College of Material Science and Chemical Engineering, Harbin Engineering University, Harbin, 15001, Heilongjiang, China*

*Corresponding author.

Tel.: +86-13059004260.

Email-address: chenye@hrbeu.edu.cn (Y Chen), wenqing@hrbeu.edu.cn (Q Wen).

**Abstract:** Sb-doped $SnO_2$ electrode was fabricated by the one-step pulse electro-codeposition method, and was modified through cerium dioxide nanoparticles (nano-$CeO_2$) doping and through cerium ion doping, respectively. The results showed that the effects of nano-$CeO_2$ doping and cerium ion doping are quite different. Nano-$CeO_2$ doping shrinks the unit cell volume, improves the degree of crystallinity and refines crystalline grains, while cerium ion doping expands the volume and deteriorates the crystallinity. Nano-$CeO_2$ doping mitigates the surface antimony enrichment and promotes the complete oxidation of antimony so that the major antimony oxidation states exist as $Sb^{5+}$ state, but cerium ion doping aggravates the enrichment and increases the $Sb^{3+}$ content. And the electrochemical phenol degradation showed that Ti/Sb-$SnO_2$-$CeO_2$ electrode has higher degradation

efficiency and its kinetic rate constant is 1.46 times as much as that of Ti/Ce-Sb-$SnO_2$. Besides, due to the compact active layer of Ti/Sb-$SnO_2$-$CeO_2$ protecting the titanium substrate from passivation, the accelerated service lifetime of Ti/Sb-$SnO_2$-$CeO_2$ is prolonged, which is 1.28 times as long as that of Ti/Ce-Sb-$SnO_2$.

**Key words:** Nano cerium dioxide; Sb-$SnO_2$; Electro-codeposition; Surface antimony enrichment.

## 1. Introduction

Titanium-based anodes, which have also been called as the dimensionally stable anodes, have been one of the greatest technological breakthroughs of electrochemistry over the last decades, and have promoted the development of electrochemistry.[1] Ti-based electrodes have been widely used in various electrochemical fields such as organic electrosynthesis, water electrolysis, chlor-alkali industry, and electrocatalytic oxidation for the organic wastewater treatment.[2,3] Among the Ti-based anodes, there are a variety of electrodes such as ruthenium dioxide ($RuO_2$), iridium dioxide ($IrO_2$), lead dioxide ($PbO_2$), manganese oxide ($MnO_2$), tin dioxide ($SnO_2$) and so on.[4] Due to the low chlorine evolution overpotential, $RuO_2$ electrode is suitable to be applied for chlorine electrolysis.[5] $IrO_2$ and $MnO_2$ electrodes are appropriately applied for water electrolysis because of their low oxygen evolution overpotential.[6,7] Antimony-doped tin dioxide (Sb-$SnO_2$) electrode has been well known for its low cost, low toxicity, and electro-generation of hydroxyl radicals[8], and is suitable to apply for the electrocatalytic organic wastewater treatment technology.

Although Sb-$SnO_2$ electrode presents a good catalytic performance, its low service life, which is due to electrode deactivation mainly caused by substrate passivation[9], seriously constrains its practicability. So a great many ideas, such as ion doping, intermediate layer insertion and so on, have been attempted to surmount this shortcoming. The idea of ion doping, including rare earth ion doping[10], noble metal ion doping[11], transition metal ion doing[12] and other ion doping[13], has been mostly put into practice through the sol-gel method, the thermal decomposition method and so on. For these methods, however, an amount of repetitive and tedious work has been done inevitably. As for the idea of intermediate layer introduction, $TiO_2$ nanotube array interlayer insertion[14], titanium nitride intermediate layer insertion[15] and so on have been attempted. $TiO_2$ nanotube array interlayer insertion and titanium nitride interlayer insertion are novel approaches and can advance the stability significantly without decreasing the activity, but have been only achieved within the lab scale and difficult to reproduce in the practical application.

Recently, for improving the electrode stability, to composite nanomaterials into active coatings by electrodeposition has become a new hot idea and only several related literatures were reported. Hu et al. have reported the impacts of carbon nanotubes and chromium carbides on Sb-$SnO_2$ electrodes.[16,17] Zhang et al. have prepared Sb-$SnO_2$ electrode modified with carbon nanotubes and have investigated the performance of electrochemical dye wastewater oxidation.[18] In our previous reports, nitrogen-doped graphene nanosheets and titanium nitrides nanoparticles were respectively used to improve the stability and catalytic activity of electrodes.[19-21]

Herein, cerium dioxide ($CeO_2$) nanoparticles are introduced to modify Sb-$SnO_2$ electrodes. Rare earth elements have been proved to enhance catalytic performance through either acting as a catalyst or assisting catalytic processes[10], thus have been widely studied to modify Sb-$SnO_2$ electrode by means of ion doping. Literatures have reported that the doping of rare earth ions into the active film can improve the surface compactness and enhance the activity for the degradation of organic contaminants.[22,23] However, the mechanism about the effects of doping rare earth ions has not been investigated in detail.

In this work, Ti/Sb-$SnO_2$-$CeO_2$ electrode was fabricated by a simple and convenient approach, one-step pulse electro-codeposition, followed by annealing at 600 °C for 2 h. Meanwhile, Ti/Ce-Sb-$SnO_2$ electrode was also prepared for the comparison. To compare the difference between cerium ion doping and nano-$CeO_2$, the morphologies, crystalline structures, surface chemical composition and catalytic activities of electrodes were investigated through scanning electron spectroscopy (SEM), transmission electron spectroscopy (TEM), X-ray diffraction (XRD), X-ray photoelectron spectrodcopy (XPS) and electrochemical measurements. During electrodeposition, $CeO_2$ nanoparticles are coated into the depositing layer, refining the depositing grains and improving the layer compactness. After annealing, a compact oxide layer with refined grains is obtained and is favorable to enhancing the electrode stability. In this way, lots of tedious work can also be avoided. And doping nano-$CeO_2$, which acts as catalyst or assisting catalyst, is advantageous to improve the catalytic activity. The modified electrode is expected to achieve enhanced stability

and activity.

## 2. Experimental

### *2.1. Preparation of electrodes*

Prior to the electrodeposition, Ti sheets (0.5 mm thickness, TA0 Type, Japan) were mechanically polished, rinsed with distilled water, and then degreased in a 10 % NaOH solution at 85 °C for 1 to 2 h. Afterward, the Ti sheets were etched in 10 % oxalic acid at 85 °C for 2 h. Finally, pretreated Ti sheets were preserved in a 3 % oxalic acid solution.

The elecrtrodeposition solution consisted of 0.1 M $SnCl_4 \cdot 5H_2O$, 0.1 M citric acid and 0.011 M $SbCl_3$. Before electrodeposition, 0.14 g cerium dioxide ($CeO_2$, 20-50 nm, analytical grade; Aladdin Chemicals, Shanghai, China) nanoparticles were mixed into the 100 mL electrodeposition solution and ultrasonically dispersed for 5 min to obtain a homogeneous suspension, and then ethylenediamine tetramethylenephosphonic acid as the additive was added dropwise to the electrolyte to obtain a 1 mM concentration. A graphite rod (spectrum grade, diameter 8 mm; Sinopharm chemical reagent Co. Ltd, Shanghai, China) was employed as the anode, whereas the Ti sheet was used as the cathode. The electrode separation distance was 1 cm. Cathodic square-wave pulse electrodeposition was performed for 0.5 h at an average current density of 5 mA $cm^{-2}$ and a bath temperature of 23 °C with the pulse conditions of 10 Hz frequency. Ti substrates with deposited layers were then dried at 100 °C and annealed in a muffle

furnace at 600 °C for 2 h. Finally, Ti/Sb-$SnO_2$-$CeO_2$ electrodes were obtained. The procedure to prepare Ti/Ce-Sb-$SnO_2$ electrode was the same as mentioned above, except adding 8 mM $Ce(NO_3)_3 \cdot 5H_2O$ instead of nano-$CeO_2$ (the concentration of Ce ions roughly equals to that of nano-$CeO_2$). And for the preparation of Ti/Sb-$SnO_2$, $CeO_2$ naoparticles were excluded.

*2.2. Characterization of electrodes*

The morphologies and crystalline patterns of Ti/Sn-$SnO_2$ and Ti/Sn-$SnO_2$-$CeO_2$ electrodes were examined by scanning electron microscope (SEM, INSPECT S50, America), field emission transmission electron microscope (FETEM, FEI TECNAI G2 F20, America), and X-ray diffractometer (XRD, Cu Kα radiation, 40 kV and 150 mA; Rigaku D/Max2500, Japan). Inductively coupled plasma mass spectroscope (ICP-MS, Xseries II, America) was performed to quantify the amounts of Sn, Sb and Ce dissolution. X-ray photoelectron spectroscope (XPS, Al Kα radiation, $h\nu$ = 1486.6 eV; Thermo ESCALAB 250, UK) was performed to analyze the composition and chemical state of the surface elements. The spectra were calibrated with respect to the signal of contamination carbon (284.6 eV) as internal reference. The XPS core level spectra were fitted and analyzed using a XPS Peak Processing program with a Lorentzian-Gaussian peak shape after a background subtraction.

*2.3. Electrochemical experiments*

A CHI760C electrochemical workstation (CH Instruments, China) was employed

to make electrochemical experiments in a conventional three-electrode system at room temperature. The as-prepared electrode served as the working electrode with a test area of 1 × 1 $cm^2$. A platinum sheet (2 × 2 $cm^2$) and saturated calomel electrode (SCE) were used as a counter and reference electrode, respectively. The supporting electrolyte was 0.25 M $Na_2SO_4$ solution. The tests were performed at room temperature. Before each measurement, the system was kept at open circuit potential for 5 - 10 min until the potential was stable. Cyclic voltammetry (CV) was performed between 0.5 and 1.5 V (vs. SCE) with different sweep rates. The accelerated service life tests were conducted using chronopotentiommetry with an anodic current density of 100 mA $cm^{-2}$. Electrochemical impedance spectroscopy (EIS) measurements were carried out in a potential of 2.0 V (vs. SCE) with a range of $10^5$ Hz - 0.1 Hz and an amplitude signal of 5 mV, and the results were fitted using the ZView program.

The electrochemical phenol degradation experiments were performed in 100 mL 100 mg $L^{-1}$ phenol solution with the supporting electrolyte of 0.25 M $Na_2SO_4$ solution. The electrolysis was performed in the galvanostatic condition of 20 mA $cm^{-2}$ with an anode area of 1 × 2 $cm^2$ and a Pt cathode area of 2 × 2 $cm^2$. Phenol solution concentrations were examined by UV-Vis spectrophotometer (Agilent UV-Vis 8453, America) using the 4-aminoantipyrine direct spectrophotometric method: 0.5 mL disposed phenol solution was added into 50 mL colorimetric cylinder, 0.5 mL ammonia buffer solution was added and mixed, and 1 mL 4-aminoantipyrine solution (2 %) and 1mL potassium ferricyanide (8 %) were added and mixed, and then the colorimetric cylinder was incubated in dark for 10 min, and finally the solution

concentration was measured by the absorbance intensity at the characteristic wavelength of 510 nm.

## 3. Results and Discussion

### *3.1. Characterization of electrodes*

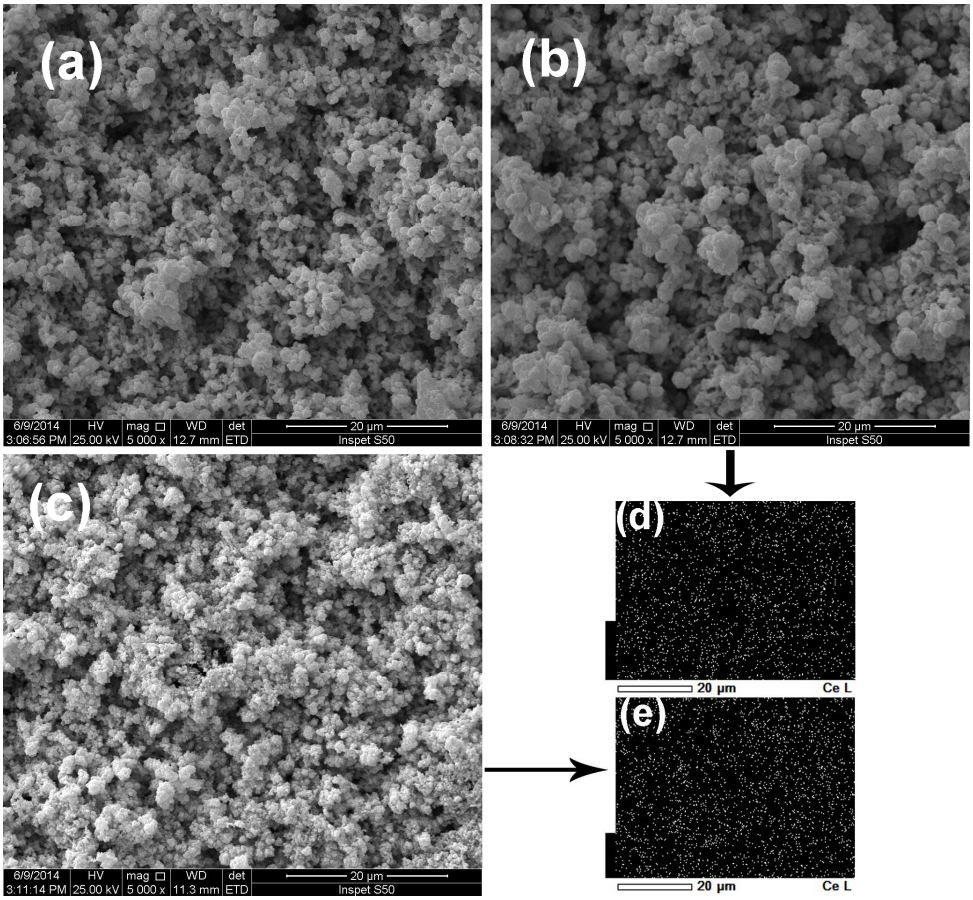


**Fig. 1** SEM images of (a) Ti/Sb-$SnO_2$, (b) Ti/Ce-Sb-$SnO_2$ and (c) Ti/Sb-$SnO_2$-$CeO_2$ electrodes; (d) and (e) element EDS mapping of Ce distribution for electrodes.

The surface morphologies of Ti/Sb-$SnO_2$, Ti/Ce-Sb-$SnO_2$ and Ti/Sb-$SnO_2$-$CeO_2$

electrodes were characterized by SEM shown in Fig. 1. The surface of active oxide layer presents a three-dimensionally microgranular layer for all electrodes. This distinct layer with uniform micropaticles can be closely related to the electrode preparation methods. Figs. 1(d) and (e) show uniform distributions of Ce element on the surfaces of active layers. Compared with Ti/Sb-$SnO_2$ and Ti/Ce-Sb-$SnO_2$ electrodes, the $CeO_2$ modified electrode presents a more compact layer with smaller microparticles. On the one hand, smaller particles have larger specific surface area and thus can provide with more catalytic active sites. On the other hand, a compact layer can protect Ti substrate from the exposed oxidization so as to improve the electrode stability. Consequently, Ti/Sb-$SnO_2$-$CeO_2$ electrode can be expected to have improved electrochemical activity and stability.

Fig. 2 displays the TEM and HRTEM images of Ti/Ce-Sb-$SnO_2$ and Ti/Sb-$SnO_2$-$CeO_2$ electrodes. Samples for the TEM were scrapped from the titanium substrate, prepared by ultrasonically dispersing the product in ethanol, and then droplets were placed on Cu grids. Figs. 2(a) and (b) show the structure with irregular particles for both electrodes. The HRTEM images of electrodes can provide more information about structure such as crystal lattice. In Fig. 2(c), two uniform interplanar distance values are 0.33 nm and 0.26 nm, which are in agreement with the (110) plane and (101) plane of tetragonal rutile $SnO_2$[24], and other two interplanar distances with values of 0.32 nm and 0.17 nm correspond to the (222) plane and (622) plane of senarmontite $Sb_2O_3$ (PDF#43-1071)[25]. This result shows the active layer of Ti/Ce-Sb-$SnO_2$ electrode has the mixed components of $SnO_2$ and $Sb_2O_3$. Fig. 2(d)

shows an interplanar distance with the value of 0.19 nm, which is in agreement with the (220) plane of cerianite $CeO_2$ (PDF#43-1002)[26]. This result shows a successful mixing of nano-$CeO_2$ into the active layer. The corresponding SAED patterns both reflect the polycrystallinity of $SnO_2$ active layers.

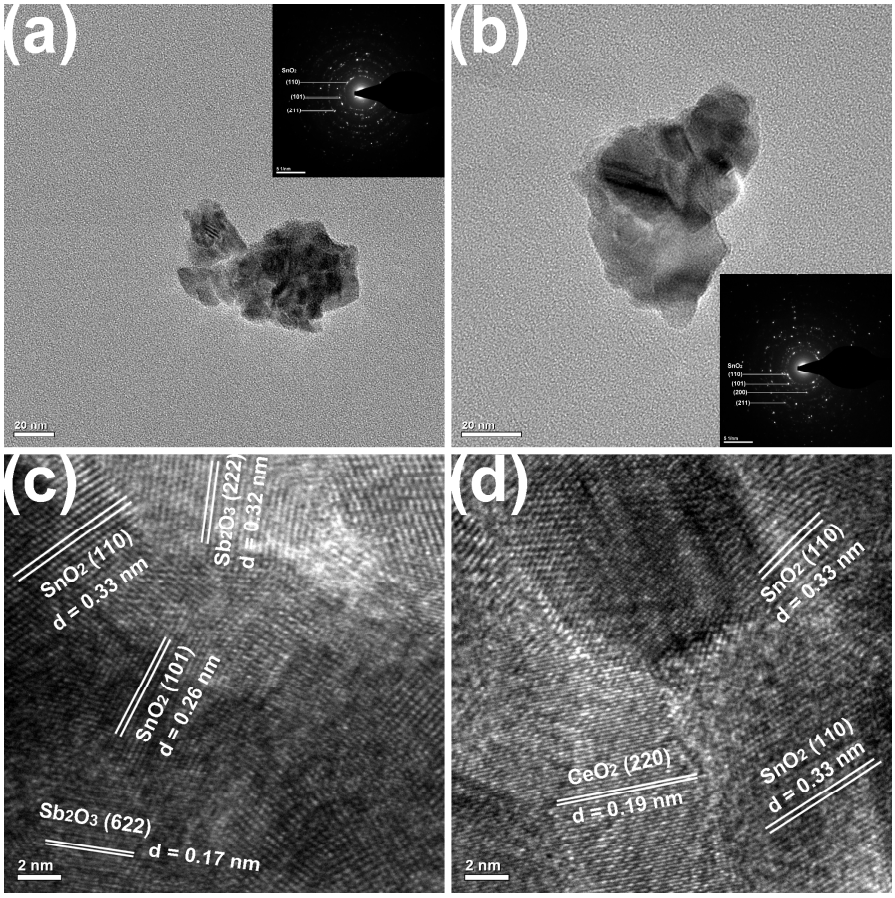


**Fig. 2** TEM images of (a) Ti/Ce-Sb-$SnO_2$ and (b) Ti/Sb-$SnO_2$-$CeO_2$ electrodes; HRTEM images of (c) Ti/Ce-Sb-$SnO_2$ and (d) Ti/Sb-$SnO_2$-$CeO_2$ electrodes. The insets are the corresponding SAED patterns.

Fig. 3 shows the XRD patterns of Ti substrate, Ti/Sb-$SnO_2$, Ti/Ce-Sb-$SnO_2$ and Ti/Sb-$SnO_2$-$CeO_2$ electrodes. The diffraction peak positions for all electrode samples coincide with those of tetragonal rutile $SnO_2$ (PDF#41-1445) with the diffraction peaks at (110), (101), (200), (211), (220), (310), (112), and (301). The strongest peak

is at (110) plane for all samples, suggesting the preferred orientation along the (110) crystallographic direction. The peak intensities of (110), (101), and (211) planes for Ti/Sb-$SnO_2$-$CeO_2$ electrode are stronger than those for Ti/Sb-$SnO_2$ electrode, indicating that the crystallinity of $SnO_2$ for Ti/Sb-$SnO_2$-$CeO_2$ electrode is better and the degree of atomic lattice is higher. However, the intensities of diffraction peaks for Ti/Ce-Sb-$SnO_2$ appear the weakest, revealing the lowest crystallinity; this can be ascribed to the effect of Ce ion doping on the nucleation process and the thermal oxidation process. This result shows that the introduction of $CeO_2$ nanoparticles is favorable to good crystallinity and ordered degree of atomic lattice. No diffraction peaks of antimony oxide and cerium oxide were found from the XRD spectra due to the low doping level (the ICP-MS results show the elemental weight percentage in Table 3). In addition, no peaks for crystallized titanium oxides are observed and only several peaks of metal titanium appear in XRD patterns of all electrodes, suggesting that the Ti substrate is not oxidized in the process of preparation and that the electro-codeposition process can produce a good protection for the Ti substrate[16,17].

To further investigate the effects of nano-$CeO_2$ doping and Ce ion doping, the lattice parameter, crystalline size, strain and texture coefficient are discussed in the following, and the analysis results are listed in Table 1.

The lattice parameters ($a$ = $b$ and $c$) for electrodes were calculated by Bragg equation based on the main diffraction peaks of rutile $SnO_2$ phase:

$$d_{hkl} = \frac{1}{\sqrt{((h^2/a^2)+(k^2/b^2)+(l^2/c^2)}} \quad (1)$$

where $d_{hkl}$ is the crystal face space, $h$, $k$ and $l$ are crystal face index, and $a$, $b$ and $c$ are

the unit-cell parameters. It is obtained that both nano-$CeO_2$ doping and Ce ion doping give rise to the increase of lattice parameter of $SnO_2$, which could be attributed to a larger radius of cerium ion than that of tin ion. Furthermore, the lattice parameters of Ti/Ce-Sb-$SnO_2$ are larger than those of Ti/Sb-$SnO_2$-$CeO_2$, which can be ascribed to more cerium ions doping into the $SnO_2$ host lattice for the cerium ion modified electrode.

The crystalline size ($D$) of the prepared powders was estimated using the Scherrer equation as follows:

$$D = \frac{0.89\lambda}{\beta \cos\theta} \quad (2)$$

where $\lambda$, $\theta$, and $\beta$ are the X-ray wavelength (0.15418 nm for Cu-Kα), Bragg diffraction angle, and the full width at half maximum intensity, respectively. Moreover, the lattice strain can be interpreted by the following equation[27]:

$$\frac{\beta \cos\theta}{\lambda} = \frac{1}{\varepsilon} + \frac{\eta \sin\theta}{\lambda} \quad (3)$$

where $\varepsilon$ and $\eta$ are the effective particle size and the effective strain. The strain can be estimated through plotting ($\beta\cos\theta/\lambda$) versus ($\sin\theta/\lambda$).

The crystalline sizes of three electrodes determined from the Scherrer equation are 35.6, 33.2, and 30.8 nm, respectively, indicating that $CeO_2$ doping can significantly refine $SnO_2$ crystalline grain. Because of the small crystalline size in nanoscale, lattice strain can be expected from the as-prepared $SnO_2$ layer. The lattice strain can be estimated from the slope of plot of ($\beta\cos\theta/\lambda$) versus ($\sin\theta/\lambda$). The values for all electrodes are -0.149, -0.141, and -0.150, respectively, indicating the presence of compressive strain in the $SnO_2$ crystal lattice. With the introduction of cerium ions,

the compressive strain in $SnO_2$ lattice increases, decreasing the compressive strain. The introduction of nano-$CeO_2$ makes a slight effect on the compressive strain, probably due to the case that cerium ions are not doped into $SnO_2$ lattice. As the doping phase, antimony ions have a smaller ion radius than tin ions and thus may cause the compressive strain in $SnO_2$ host lattice. It can be assumed that the doping of antimony ions with smaller ion radius into the $SnO_2$ host lattice results in the compression of $SnO_2$ lattice but that the doping of cerium ions makes the effect of swelling strain. This assumption is also confirmed by the results.

In addition, the texture coefficient ($P_{(hkl)}$) is also employed to determine the preferred crystalline orientations. $P_{(hkl)}$ is defined as[28]:

$$P_{(h_ik_il_i)} = \frac{I_{(h_ik_il_i)}/I_{0(h_ik_il_i)}}{(1/n)\sum I_{(h_ik_il_i)}/I_{0(h_ik_il_i)}} \quad \text{for } i = 1, 2, 3\ldots, \text{n} \qquad (4)$$

where $I_{(hkl)}$ and $I_{0(hkl)}$ are the diffraction intensities of the ($hkl$) plane for measured sample and standard sample, respectively. Only three main diffraction peaks of electrode samples, i.e. (110), (101) and (211), are considered, and the obtained texture coefficients are listed in Table 1. Ti/Sb-$SnO_2$ electrode presents a significant preferred crystalline orientation along the (110) direction. However, Ti/Ce-Sb-$SnO_2$ presents a decreased preferred orientation along the (110) and (101) directions but an increase along the (211) direction, while Ti/Sb-$SnO_2$-$CeO_2$ appears the least significant preferred crystalline orientation and closest to the standard $SnO_2$ crystalline orientation.

In summary, the introduction of nano-$CeO_2$ plays a role in refining crystalline grains and improving the crystallinity, while doping of cerium ions into the $SnO_2$ host

lattice improves the preferred orientation along the (211) direction, decreases the compressive strain in the lattice, and increases the unit cell volume. These results can make important effects on the properties of electrodes.

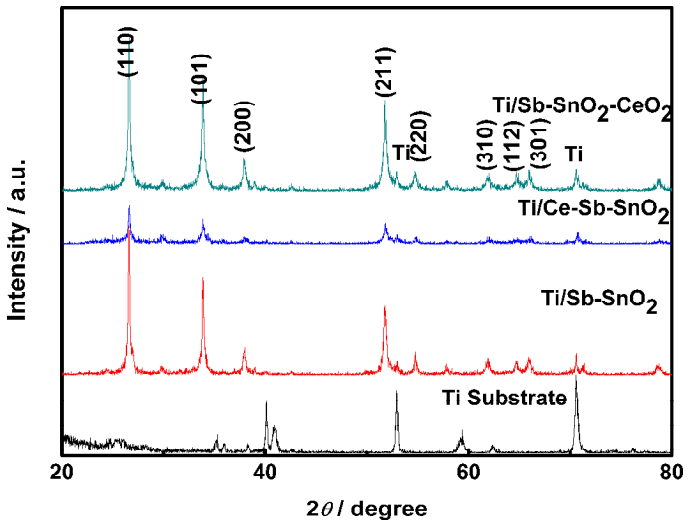


**Fig. 3** XRD patterns of Ti substrate, and Ti/Sb-$SnO_2$, Ti/Ce-Sb-$SnO_2$ and Ti/Sb-$SnO_2$-$CeO_2$ electrodes.

**Table 1** XRD analysis results of electrodes.

| Electrode sample | Unit cell parameter | | | relative texture coefficient | | | Crystal size | Strain |
|---|---|---|---|---|---|---|---|---|
| | *a*=*b* (Å) | *c* (Å) | *V* (Å$^3$) | (110) | (101) | (211) | / nm | |
| Ti/Sb-$SnO_2$ | 4.802 | 3.375 | 77.82 | 1.14 | 0.97 | 0.89 | 35.6 | -0.149 |
| Ti/Ce-Sb-$SnO_2$ | 4.835 | 3.372 | 78.82 | 1.06 | 0.93 | 1.01 | 33.2 | -0.141 |
| Ti/Sb-$SnO_2$-$CeO_2$ | 4.805 | 3.378 | 77.99 | 1.00 | 1.00 | 1.00 | 30.8 | -0.150 |

XPS measurements of electrodes were conducted to analyze the chemical states of elements (shown in Fig. 4). Fig. 4(a) shows the XPS survey scan of

Ti/Sb-$SnO_2$-$CeO_2$ electrode. Sample has Sn, Sb, Ce, O and C. The presence of C 1s results from the organic carbon contamination. Considering the effect of doping $CeO_2$ nanoparticles and doping cerium ions, further investigations were carried out. A comparison of the Sn 3d spectra of Ti/Sb-$SnO_2$, Ti/Ce-Sb-$SnO_2$ and Ti/Sb-$SnO_2$-$CeO_2$ electrodes was shown in Fig. 4(b). The spectra reveal the spin-orbit of Sn $3d_{5/2}$ ground state to be around 486.7 eV while the Sn $3d_{3/2}$ excited state is observed around 495.1 eV (Table 2), which is ascribed to $Sn^{4+}$ in $SnO_2$. The gap between the Sn $3d_{5/2}$ and Sn $3d_{3/2}$ levels is about 8.4 eV, which closely corresponds to the O in $SnO_2$ and Sn in $SnO_2$, respectively.[29] Fig. 4(c) shows the Ce 3d spectra of Ti/Ce-Sb-$SnO_2$ and Ti/Sb-$SnO_2$-$CeO_2$ and demonstrates the successful introduction of nano-$CeO_2$ or cerium ions into the deposit layer.

The XPS spectra of Sb $3d_{5/2}$ and O 1s are overlapped, thus they were fitted using XPS Peak Processing Program, the Sb $3d_{5/2}$ peak is separated from the mixed spectrum (Sb $3d_{5/2}$ plus O 1s), and the results are shown in Figs. 4(d), (e) and (f). Then the O 1s peak is split into two peaks and fitted values are given in Table 2. Generally, the O 1s peak has been observed at 529 - 535 eV. And the O 1s peak is fitted into two peaks at 530.2-530.3 eV and 531.1-532.9 eV, respectively. The peak at the low binding energy region has been attributed to lattice oxygen species ($O_{lat}$) which are incorporated into $SnO_2$ crystal lattice, and the peak at the high binding energy region has been ascribed to adsorbed hydroxyl oxygen containing species ($O_{ads}$) which are adsorbed hydroxyl group.[30] For the Sb $3d_{3/2}$ peak, the intensity for Ti/Sb-$SnO_2$-$CeO_2$ is very slight, which is quite different from that of Ti/Sb-$SnO_2$ and

that of Ti/Ce-Sb-$SnO_2$. This situation may be due to the case that the major antimony oxidation states exist as $Sb^{5+}$ state.[31] To investigate the chemical states of antimony element on the electrode surface, the peak of Sb $3d_{3/2}$ is split into two peaks to character $Sb^{5+}$ and $Sb^{3+}$. The peak of $Sb^{3+}$ appears at the low binding energy region, and the peak of $Sb^{5+}$ at the high binding energy region.

It is seen from Table 2 that the atom ratio of Sn: Sb is at 6.0 - 7.1. The doping of cerium ions causes a decrease for the atom ratio of Sn: Sb, showing an increased content of antimony element on the electrode surface. But Ti/Sb-$SnO_2$-$CeO_2$ presents a decreased content of antimony. This phenomenon is probably due to the antimony surface enrichment at high temperature.[32] What is possible, antimony and cerium ions competitively doping into the $SnO_2$ host crystalline lattice intensifies the enrichment of antimony on the electrode surface, while the introduction of nano-$CeO_2$ suppresses the antimony enrichment, decreases the surface antimony content and thus benefits to the surface antimony oxidation. Table 3 shows the ICP-MS result and gives the overall weight percentages of individual elements in the as-prepared materials. Observed from the ICP-MS result, the overall atom ratio of Sn and Sb is significantly more than that of XPS result, demonstrating the above analysis. To further investigate the surface antimony states, the Sb $3d_{3/2}$ peak is split and analyzed, and the atom ratio of $Sb^{5+}$: $Sb^{3+}$ is obtained. For the Ti/Sb-$SnO_2$ and Ti/Ce-Sb-$SnO_2$ samples, $Sb^{5+}$ and $Sb^{3+}$ coexist on the surface, while $Sb^{5+}$ as the major antimony oxidation state exists on the surface for Ti/Sb-$SnO_2$-$CeO_2$ sample. Hence the introducing of nano-$CeO_2$ promotes the complete oxidation of antimony in the deposit layer. This result shows

that doping cerium ions and doping nano-$CeO_2$ make distinctively different effects on the surface antimony states, which can be expected to have effects on the electrocatalytic activity of as-prepared electrodes for removal of organic contaminants. The atom ratio of $O_{ads}$: $O_{lat}$ for Ti/Ce-Sb-$SnO_2$ is higher than that of Ti/Sb-$SnO_2$, and it is the highest for Ti/Sb-$SnO_2$-$CeO_2$, implying that the catalytic activity of electrode will be considerably influenced by doping $CeO_2$ nanoparticles.

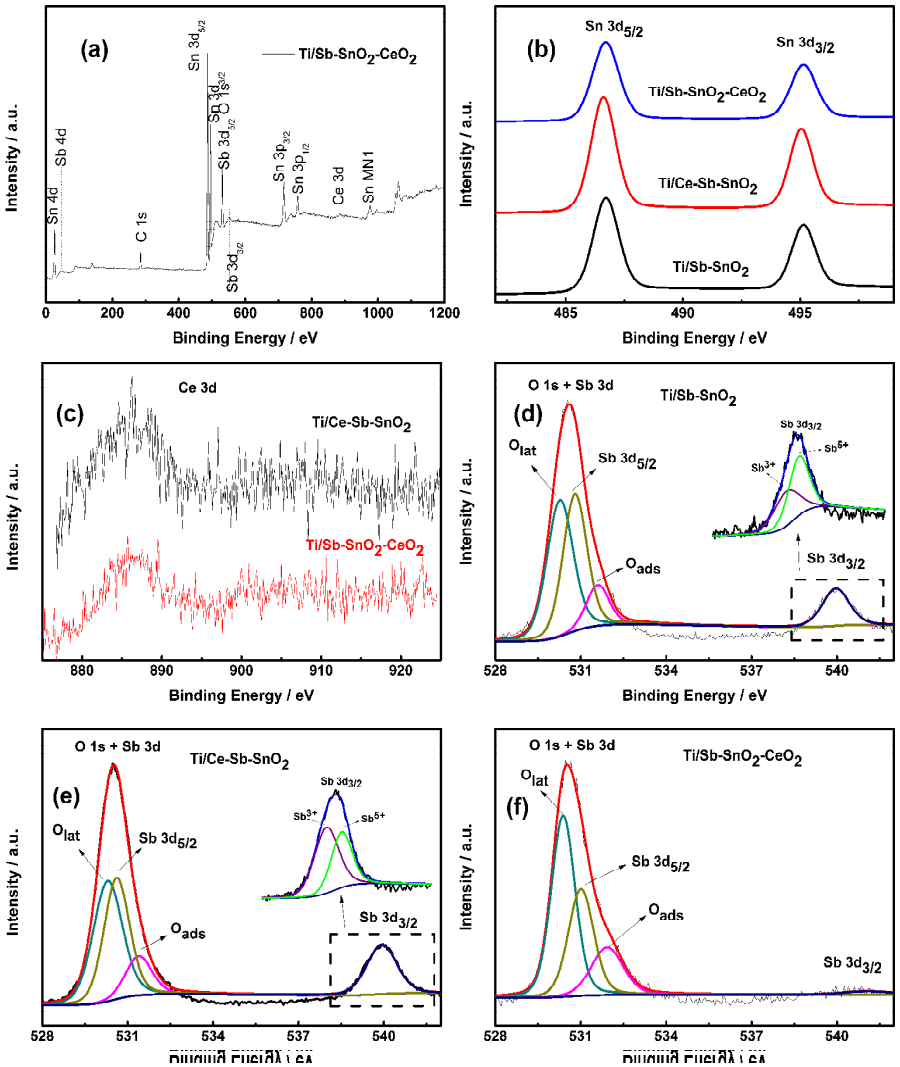


**Fig. 4** XPS spectra: (a) survey scanning spectrum, and (b) Sn 3d and (c) Ce 3d spectra of electrodes; O 1s and Sb 3d spectra on the surfaces of (d) Ti/Sb-$SnO_2$, (e) Ti/Ce-Sb-$SnO_2$ and (f) Ti/Sb-$SnO_2$-$CeO_2$

electrodes.

**Table 2** XPS analysis results of electrodes.

| Electrode sample | Binding Energy / eV | | | | | Atom ratio | | |
|---|---|---|---|---|---|---|---|---|
| | Sn $3d_{5/2}$ | Sn $3d_{3/2}$ | Sb $3d_{3/2}$ | $O_{ads}$ | $O_{lat}$ | Sn: Sb | $Sb^{5+}$: $Sb^{3+}$ | $O_{ads}$: $O_{lat}$ |
| Ti/Sb-$SnO_2$ | 486.7 | 495.2 | 540.0 | 531.6 | 530.3 | 6.5 | 1.4 | 0.26 |
| Ti/Ce-Sb-$SnO_2$ | 486.6 | 495.1 | 539.9 | 531.2 | 530.2 | 6.0 | 0.71 | 0.29 |
| Ti/Sb-$SnO_2$-$CeO_2$ | 486.7 | 495.1 | 541.0 | 531.8 | 530.3 | 7.1 | -- | 0.35 |

**Table 3** Chemical composition results of electrode active layers.

| Sample | Ce / wt% | Sb / wt% | Sn / wt% | Atom ratio of Sn: Sb |
|---|---|---|---|---|
| Ti/Ce-Sb-$SnO_2$ | 0.51% | 8.22% | 91.28% | 11.4 |
| Ti/Sb-$SnO_2$-$CeO_2$ | 0.62% | 7.89% | 91.49% | 11.9 |

Based on the XRD, XPS and ICP-MS analysis results, a schematic illustration is given out to explain the effects of nano-$CeO_2$ introducing on the electrode surface. In metal oxides, extrinsic aliovalent substitutional doping is widely employed to produce doped conductors for tuning the properties of semiconductor.[33] In this approach, the lattice atom is substituted by extrinsic atom with higher or lower valence, introducing shallow electron or hole states into the band structure so as to modify the material performance. In our work, the effects of nano-$CeO_2$ doping and cerium ion doping are investigated. When antimony ions are doped into $SnO_2$ phase, the surface of $SnO_2$

electrode presents the coexistence of $Sb^{5+}$ and $Sb^{3+}$ states after annealing at high temperature. With antimony and cerium ions being simultaneously introduced, antimony and cerium are competitively doped into the $SnO_2$ host lattice so as to aggravate the surface antimony enrichment and increases significantly the content of $Sb^{3+}$. In contrast, the introduction of nano-$CeO_2$ mitigates the surface antimony enrichment and promotes the complete oxidation of antimony so that the major antimony oxidation states exist as $Sb^{5+}$ state. These indicate that cerium ion doping and nano-$CeO_2$ doping make very different effects. The doping properties of materials can make an important contribution to the oxygen activity, which means influencing the content of adsorbed hydroxyl oxygen containing species on the surface and then determines the electrode activity. Next, the effects on electrocatalytic activity of electrodes will be studied.

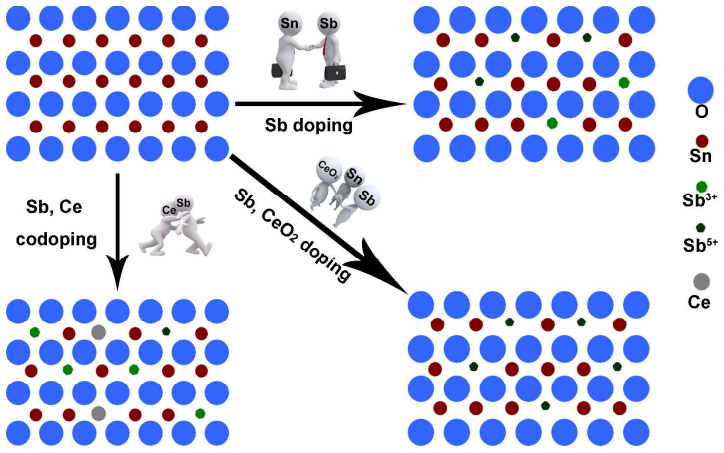


**Scheme 1** Schematic representation for the effects of cerium ion doping and nano-$CeO_2$ doping.

*3.2. Electrocatalytic performance of electrodes towards phenol*

The electrochemical organic degradation experiment have been the most direct and practicable method to investigate the catalytic ability of electrode for the removal of organic contaminants. As shown in Fig. 5, the electrochemical phenol degradation processes were performed on Ti/Sb-$SnO_2$, Ti/Ce-Sb-$SnO_2$ and Ti/Sb-$SnO_2$-$CeO_2$ electrodes, respectively. Observed from Fig. 5(a), the removal efficiencies of phenol increase with electrolysis time. The degradation on Ti/Ce-Sb-$SnO_2$ is more efficient than that on Ti/ Sb-$SnO_2$, and Ti/Sb-$SnO_2$-$CeO_2$ is the most efficient among all samples. After 4 h electrolysis, the phenol removal efficiencies are 81.3 %, 84.2 % and 90.7 %, respectively, revealing that the electrocatalytic ability of Ti/Sb-$SnO_2$-$CeO_2$ electrode is the highest. Fig. 5(b) shows the logarithmic relationship of phenol concentration with electrolysis time, and the fitting degrees of curves are above 0.99. Therefore, the phenol degradation process follows the pseudo-first-order kinetics model:

$$dc / dt = -kc \qquad (5)$$

where $c$ is the phenol concentration at given time and $k$ is the kinetic rate constant. The kinetic rate constants for phenol degradation were obtained from the slope of $\ln(c_0/c)$ versus electrolysis time curves in Fig. 5(b), and they are 0.490 $h^{-1}$, 0.526 $h^{-1}$ and 0.715 $h^{-1}$, respectively. The removal rate constant on Ti/Sb-$SnO_2$-$CeO_2$ is 1.46 and 1.36 times as much as that for Ti/Sb-$SnO_2$ and that for Ti/Ce-Sb-$SnO_2$, respectively. This shows that phenol can be removed most efficiently on Ti/Sb-$SnO_2$-$CeO_2$ electrode, which can be explained by the high ratio of $O_{ads}$: $O_{lat}$.

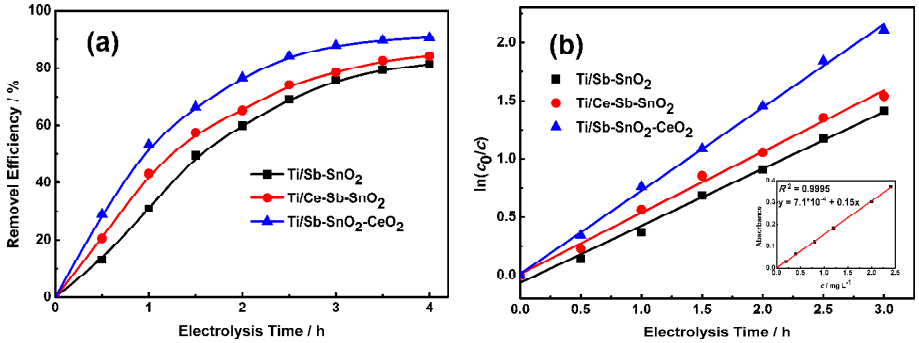


**Fig. 5** Electrochemical degradation of phenol (100 mg $L^{-1}$) on Ti/Sb-$SnO_2$, Ti/Ce-Sb-$SnO_2$, and Ti/Sb-$SnO_2$-$CeO_2$ electrodes with a current density of 20 mA $cm^{-2}$. (a) Variations of removal efficiency with electrolysis time, and (b) the pseudo-first-order kinetics curves of phenol degradation. The inset is the calibration curve of phenol solution. The supporting electrolyte is 0.25 M $Na_2SO_4$ solution.

### *3.3. Voltammetric Characterization*

In order to explain the effect of doping nano-$CeO_2$ on the electrocatalytic activity of electrodes, the roughness factor and voltammetric charge of all electrodes were determined from the cyclic voltammetry (CV). Both roughness factor reflecting the real surface area of electrode, and voltammetric charge related to the amounts of electroactive sites, are some of factors to determine electrocatalytic activity.[11]

The roughness factor is defined as real surface area per apparent geometric area of electrode, and calculated through comparing determined capacitance with the capacitance of a smooth oxide surface (8 μF $cm^{-2}$).[34] Figure 6(a) shows some cyclic voltammograms recorded at different scan rates between 5 and 200 mV $s^{-1}$ in 0.25 M $Na_2SO_4$ solution from 0.7 to 0.8 V (vs. SCE), and only double-layer charging currents

were observed. The current densities of Fig. 6(b) were measured in the points of 0.75 V from the CVs for different sweep rates (see Fig. 6(a), and Fig. S1(a) and (b)). The linear relationship between current density and sweep rate confirms the nonfaradaic character of current in this potential region.[35] The capacitances were obtained from the plot slopes in Fig. 6(b), and they were compared with the value of 8 μF $cm^{-2}$ to estimate the roughness factor. The results are 42, 90 and 142. Compared with that of Ti/Sb-$SnO_2$, the roughness factor of Ti/Sb-$SnO_2$-$CeO_2$ is boosted (142 versus 42). Thus, the introduction of $CeO_2$ nanoparitcles can improve remarkably the roughness of electrode surface and is favorable to the electrocatalytic activity.

The voltammetric charge ($q^*$) is closely related to the real specific surface area and the amounts of electroactive sites, which greatly determines the electrocatalytic performance of electrode.[36] The total voltammetric charge $q_T^*$, which is related to the total electrochemically active surface area of the oxide coating, can be obtained through plotting the reciprocal of $q^*$ against the square root of the potential scan rate by using the following equation:[37]

$$1/q^* = 1/q_T^* + kv^{1/2} \qquad (6)$$

The outer voltammetric charge $q_O^*$, which is the charge related to the most accessible electroactive surface area, is obtained according to the following equation:

$$q^* = q_O^* + k'v^{-1/2} \qquad (7)$$

Figs. 6(c) and (d) show voltammetric charge plots (they are obtained through plotting the voltammetric results in Figs. S1(c), (d) and (e)) for Ti/Sb-$SnO_2$, Ti/Ce-Sb-$SnO_2$ and Ti/Sb-$SnO_2$-$CeO_2$ electrodes, and linear fittings can be observed.

The calculated results of total voltammetric charge are 2.55, 2.64 and 2.75 mC $cm^{-2}$, respectively, and the results of outer voltammetric charge are 1.08, 1.48 and 1.60 mC $cm^{-2}$, respectively. These show that the outer voltammetric charge of Ti/Sb-$SnO_2$-$CeO_2$ is 1.48 and 1.08 times as much as that of Ti/Sb-$SnO_2$ and that of Ti/Ce-Sb-$SnO_2$, respectively. This result confirms that Ti/Sb-$SnO_2$-$CeO_2$ electrode possesses the best electrocatalytic activity.

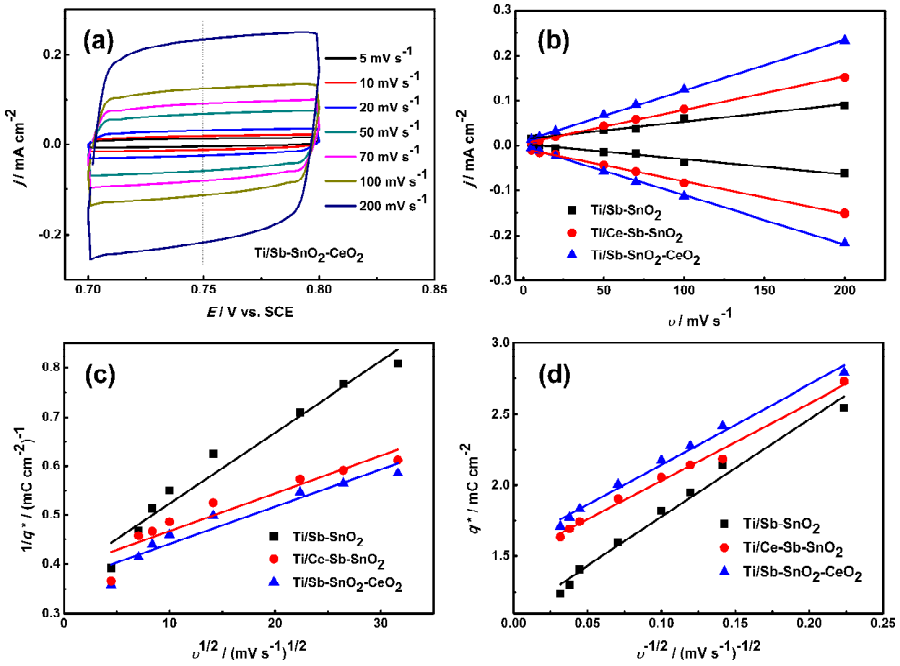


**Fig. 6** (a) Cyclic voltammgrams between 0.7 and 0.8 V at different sweep rates for Ti/Sb-$SnO_2$-$CeO_2$ in 0.25 M $Na_2SO_4$ solution. (b) Evolution of the current density at 0.75 V versus the sweep rate. (c) Reciprocal voltammetric charge ($1/q^*$) versus the square root of the voltammetric scan rate ($v^{1/2}$). (d) Voltammetric charge ($q^*$) versus the reciprocal square root of the voltammetric scan rate ($v^{-1/2}$). (c) and (d) data was obtained from the cyclic voltammograms between 0.5 and 1.5 V (vs. SCE) at various scan rates in 0.25 M $Na_2SO_4$ solution.

*3.5. Electrode stability*

Electrodes are investigated through accelerated service life experiments to compare their stabilities. At a high current density, the severe oxygen evolution reaction occurring on the electrode surface aggravates the electrode deactivation. Fig. 7 shows the accelerated service life curves of electrodes. The anode potential is recorded as a function of time, and it indicates that the electrode is deactivated when the potential increases steeply. Ti/Sb-$SnO_2$ electrode displayed a continuous increase by 5 V in potential and got deactivated within 5.3 h. Ti/Ce-Sb-$SnO_2$ demonstrated the similar tendency with Ti/Sb-$SnO_2$-$CeO_2$ in the potential variation with electrolysis time except a small step change from 3.5 V to 3.8 V. And the potential of Ti/Sb-$SnO_2$-$CeO_2$ electrode showed a slow increase with an S-type change. Base on the above situation, the accelerated service life for Sb-doped $SnO_2$ electrodes is defined as the time at which the potential reaches a value of 5.0 V.[14] As observed from Fig. 7, the accelerated service lives of Ti/Sb-$SnO_2$ and Ti/Ce-Sb-$SnO_2$ electrodes are 5.3 h and 6.8 h, respectively. And the accelerated life of $CeO_2$ modified electrode is prolonged to 8.7 h, which is 1.28 times as much as that of cerium ion doped electrode. The improved accelerated lifetime can be ascribed to the compact active layer with small crystalline grain size caused by the introduction of $CeO_2$ nanoparticles. The electrode deactivation process will be discussed in the following section.

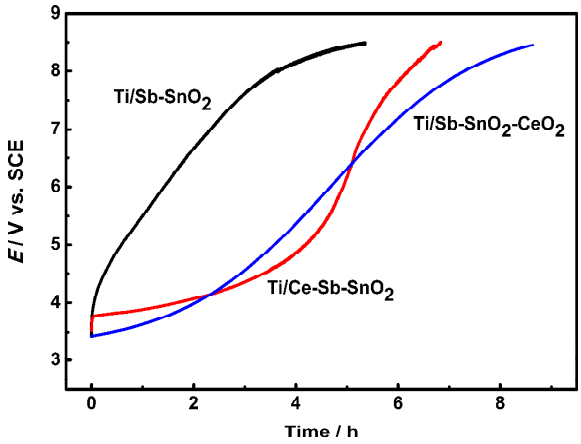


**Fig. 7** Accelerated service life tests on Ti/Sb-$SnO_2$, Ti/Ce-Sb-$SnO_2$ and Ti/Sb-$SnO_2$-$CeO_2$ electrodes in a 0.25 M $Na_2SO_4$ solution with a constant anodic current density of 100 mA $cm^{-2}$.

*3.6. EIS Characterization*

Herein, EIS experiments were performed with a potential of 2.0 V in 0.25 M $Na_2SO_4$ solution. Fig. 8 shows the EIS spectra for Ti/Sb-$SnO_2$, Ti/Ce-Sb-$SnO_2$ and Ti/Sb-$SnO_2$-$CeO_2$ electrodes. In order to depict the electrochemical behaviors of electordes, the equivalent circuit was used to fit and to model the EIS behavior shown in the inset of Fig. 8(a). The Nyquist plots for all electrodes are similar in form, present two electrochemical processes, and can be characterized by one resistance in the high frequency region, one capacitive-resistive semicircle in the middle frequency region and one depressed capacitive-resistive semicircle in the low frequency region. As shown in Fig. 8(b), the semicircle in the middle frequency region remains constant with potential, while the depressed semicircle in the low gradually shrinks. Considering the electrochemical system in this paper, there are several possible

explanations for this situation.

One of possibilities is electrode porosity, meaning that pores and cracks may provide an alternative pathway for faradaic current.[38] However, the charge transfer resistances for both processes should decrease with potential, which is not consistent with the observation. Other possibility is the brick model reported by Díaz-Flores et al..[39] In a polycrystalline material, a stereo-network of crystal grains separated by the grain boundaries is formed, and grains and grain boundaries are associated different resistivity: the middle frequency semicircle is owed to the grains and the low frequency one with the grain boundaries. However, there is no reasonable statement for the constant resistance of middle frequency semicircle. Additionally, a faradaic reaction along with adsorption and desorption of the reaction intermediates generated through the oxygen evolution reaction process[40], can be also likely to explain the electrochemical processes. In the model, the middle frequency semicircle is rather stable with potential and acts as a constant parallel *RC* element in series with the oxygen evolution process. Here, the electrochemical processes in our work are well consistent with the adsorption-desorption model.

The resistance in the high frequency corresponds to resistance ($R_1$) in the model and represents the solution resistance caused by the concentration polarization process. The semicircle in the middle frequency corresponds to the capacitance ($C_2$) and resistance ($R_2$) in the model, represents the first electrochemical process. It is supposed to represents the electrochemical behavior of the growth of a resistive hydrated layer at the oxide/solution interface and is rather stable with the potential.[40]

However, the resistive hydrated layer is not well understood. Among the electrodes for electrochemical wastewater treatment, $SnO_2$ electrode is well known for the electro-generation of hydroxyl radicals. Thus it is a plausible assumption that the first semicircle can be derived from adsorption and desorption of hydroxyl radicals. Observed from Table 4, Ti/Sb-$SnO_2$-$CeO_2$ electrode has a smallest $R_2$ value,

The depressed semicircle in the low frequency region, which behaves as the constant phase element ($CPE_3$) and charge transfer resistance ($R_3$) in the equivalent circuit, represents the electrochemical discharge process. It results from the frequency dispersion which is presented by a *CPE* and possibly caused by different physicochemical phenomena. Pajkossy deemed that the *CPE* behavior was mainly caused by the local variations of electrode capacitance which was due to atomic scale inhomogeneity, different crystal structures or defects, and surface adsorption.[41] Costa et el. deemed that the *CPE* behavior was induced by electrode surface morphology such as roughness, porosity, nonuniformity.[42] And the major factor causing *CPE* behaviors during the oxygen evolution was the adsorption of reaction intermediates. Analysis of XRD results reveal that doping antimony element leading to $SnO_2$ lattice defects, applying current pulse, and introducing nano-$CeO_2$ bring about cell volume contraction. And as-prepared electrodes present rough surface. These induce the *CPE* behavior of Sb-doped $SnO_2$ electrodes.

The behavior of second semicircle demonstrates the electrochemical performance of electrodes. A low charge transfer resistance (corresponding to $R_3$) can reflect a good electrochemical activity. The $R_3$ value of Ti/Sb-$SnO_2$-$CeO_2$ electrode is only

12.52 ohm while that for Ti/Ce-Sb-$SnO_2$ electrode is 20.03 ohm (Table 4), showing a prominent improvement of electrochemical performance for electrodes. This result reveals the contribution of nano-$CeO_2$ to the improved electrode activity.

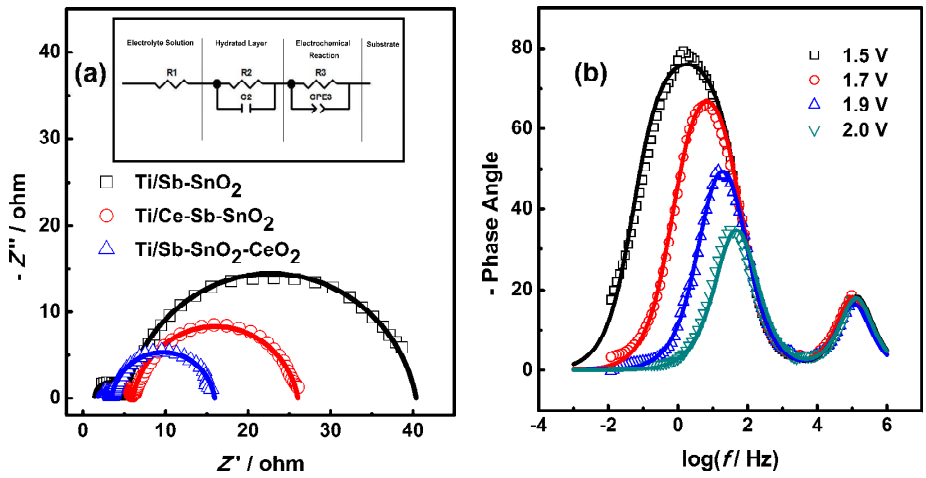


**Fig. 8** (a) Nyquist plots of Ti/Sb-$SnO_2$ and Ti/Sb-$SnO_2$-$CeO_2$ electrodes obtained at 2.0 V, the inset is corresponding equivalent circuit model. (b) Bode plots for Ti/Sb-$SnO_2$-$CeO_2$ electrode at different potentials.

To understand the failure mechanism and the effect of nano-$CeO_2$ doping, we did further EIS for deactivated electrodes. The electrode deactivation can be understood: during the accelerated life test, the intense generation of oxygen bubbles occurs on the electrode surface, and it leads to the consumption of catalytic layer and/or the formation of an insulating $TiO_2$ layer between the Ti substrate and the catalyst layer; the formation of $TiO_2$ layer is the main cause of the electrode deactivation.[14,35,43]

Fig. 9 shows the EIS spectra of deactivated electrodes. Similarly, the electrode process consists of one concentration polarization process and two electrochemical reaction processes. Deactivated Ti/Sb-$SnO_2$-$CeO_2$ electrode displays the behaviors of hydrated layer and deactivated $SnO_2$ layer, indicating only the loss of electrochemical

activity. However, differing from the situation of deactivated Ti/Sb-$SnO_2$-$CeO_2$, the middle frequency semicircles of other deactivated electrodes present depressed, and the charge transfer resistances ($R_3$) significantly increase by more than one order of magnitude, indicating the electrochemical reaction occurring on the mediated oxide layer which results from the substrate oxidation.

The equivalent circuit model in Fig. 8 is still available to depict the electrochemical behavior on the surface of deactivated Ti/Sb-$SnO_2$-$CeO_2$. For the deactivated $CeO_2$-modified electrode, the semicircle in the middle frequency can be explained by the resistive hydrated layer due to its being not significantly changed and independent of the potential. However, for the deactivated Ti/Sb-$SnO_2$ and Ti/Ce-Sb-$SnO_2$, the electrochemical impedance in the middle frequency is not suitable any longer to be explained as the effect of resistive hydrated layer but the electrochemical process on the mediated oxide layer caused by the titanium substrate passivation. The analysis demonstrates that the deactivation of Ti/Sb-$SnO_2$-$CeO_2$ mainly results from the active layer consumption while the deactivation of Ti/Sb-$SnO_2$ and Ti/Ce-Sb-$SnO_2$ is ascribed to the consumption of catalyst layer and the passivation of titanium substrate. Therefore, the introduction of $CeO_2$ nanoparticles into the active layer can effectively protect the substrate from passivation.

Based on the above analysis results, Scheme 2 is drawn to describe the electrocatalytic phenol degradation process on Ti/Sb-$SnO_2$-$CeO_2$ electrode. On one hand, Ti/Sb-$SnO_2$-$CeO_2$ electrode possesses a high activity to electro-generate

hydroxyl radicals as the strong oxidizing species for the degradation of phenol in the aqueous solution. On the other hand, it has a compact $SnO_2$ active layer to protect the substrate from passivation, showing a good stability.

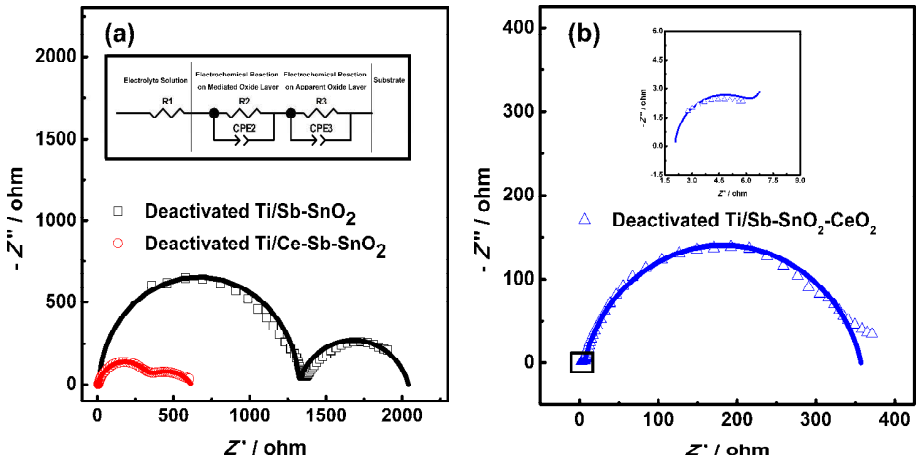


**Fig. 9** Nyquist plots of (a) deactivated Ti/Sb-$SnO_2$ and Ti/Ce-Sb-$SnO_2$ electrodes, and (b) deactivated Ti/Sb-$SnO_2$-$CeO_2$ electrodes.

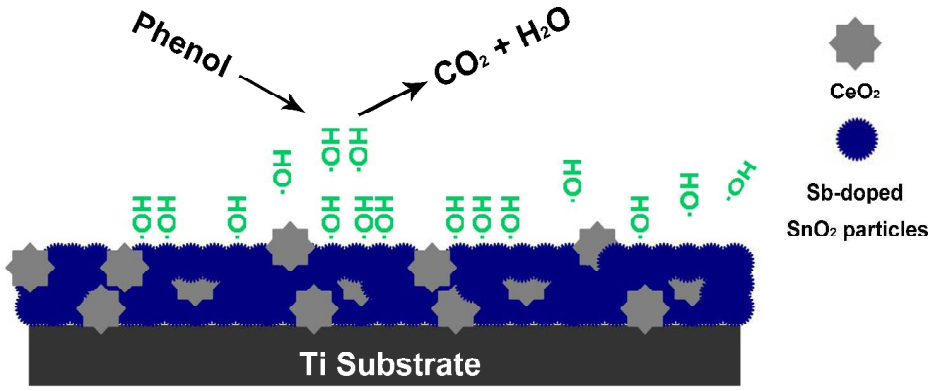


**Scheme 2** Schematic representation for the electrocatalytic phenol degradation on Ti/Sb-$SnO_2$-$CeO_2$ electrode.

**Table 4** EIS fitting results of active electrodes and deactivated electrodes.

| Electrode | $R_1$/ohm | $R_2$/ohm | $CPE_2$/F | $n_2$ | $R_3$/ohm | $CPE_3$/F | $n_3$ |
|---|---|---|---|---|---|---|---|

| | | | | | | | |
|---|---|---|---|---|---|---|---|
| Ti/Sb-$SnO_2$ | 1.42 | 3.71 | $8.03\times10^{-7}$ | 1.00 | 35.24 | $1.55\times10^{-3}$ | 0.88 |
| Ti/Ce-Sb-$SnO_2$ | 2.71 | 3.31 | $2.97\times10^{-7}$ | 1.00 | 20.03 | $1.15\times10^{-3}$ | 0.88 |
| Ti/Sb-$SnO_2$-$CeO_2$ | 1.82 | 1.61 | $1.04\times10^{-6}$ | 1.00 | 12.52 | $1.21\times10^{-3}$ | 0.90 |
| Deactivated Ti/Sb-$SnO_2$ | 13.9 | 1447 | $5.18\times10^{-9}$ | 0.91 | 723 | $3.81\times10^{-5}$ | 0.82 |
| Deactivated Ti/Ce-Sb-$SnO_2$ | 4.85 | 313 | $2.18\times10^{-5}$ | 0.87 | 320 | $2.14\times10^{-5}$ | 0.60 |
| Deactivated Ti/Sb-$SnO_2$-$CeO_2$ | 2.07 | 4.30 | $9.04\times10^{-7}$ | 1.00 | 350 | $4.77\times10^{-5}$ | 0.86 |

## 4. Conclusions

Ti/Sb-$SnO_2$ electrode modified with $CeO_2$ nanoparticles was successfully fabricated by the one-step electro-codeposition method. The influence of $CeO_2$ nanoparticles were investigated through SEM, TEM, XRD, XPS, and electrochemical measurements. Compared with Ti/Sb-$SnO_2$ and Ti/Ce-Sb-$SnO_2$, Ti/Sb-$SnO_2$-$CeO_2$ electrode has smaller crystalline grain size and compact layer which can provide with more active sites. The kinetic analysis of electrochemical phenol degradation shows that the degradation process of phenol coincides with the pseudo-first-order kinetics and that the rate constant on Ti/Sb-$SnO_2$-$CeO_2$ electrode is 0.715 $h^{-1}$, 1.46 times as much as that on Ti/Sb-$SnO_2$. Voltammetric characterization results show that Ti/Sb-$SnO_2$-$CeO_2$ electrode possesses larger roughness factor and higher specific voltammetric charge for electrocatalytic phenol degradation, explaining the improved electrocatalytic activity of $CeO_2$-modified electrode and the contribution of introducing $CeO_2$ nanoparticles. At last, the deactivation analysis through the

impedance spectroscopy indicates that the introduction of nano-$CeO_2$ improves the compactness of active layer to protect electrode from the substrate passivation, and thus enhances the electrode stability. Therefore, the $CeO_2$-modified Ti/Sb-$SnO_2$ electrode presents a high electrocatalytic activity and good stability.

## Acknowledgements

This work was supported by National Natural Science Foundation of China (No. 51179033 and No. 21476053), the Doctoral Program of the Ministry of Education (No. 20132304110027), the Fundamental Research Funds for the Central Universities (HEUCF201403019), Heilongjiang Postdoctoral Science Research Foundation (LBH-Q12118), and Special Fund Research Program for Talents of Science Technology Innovation in Harbin (No. 2009RFXXG204).

## References

[1] S. Trasatti, The electrochemistry of novel materials; J.Lipkowski, P. N. Ross, Eds.; VCH Publishers: New York, 1994.

[2] S. Trasatti, Electrocatalysis: understanding the success of DSA, *Electrochim. Acta*, 2000, **45**, 2377-2385.

[3] A. N. S. Rao, V. T. Venkatarangaiah, Metal oxide-coated anodes in wastewater treatment, *Environ. Sci. Pollut. R.*, 2014, **21**, 3197-3217.

[4] J. Kristóf, E. Horváth, S. Daolio, Study of metal oxide electrocatalytic thin film

evolution by thermoanalytical and spectroscopic techniques-a review, *Electrocatalysis*, 2013, **4**,196-202.

[5] V. Trieu, B. Schley, H. Natter, J. Kintrup, A. Bulan, R. Hempelmann, $RuO_2$-based anodes with tailored surface morphology for improved chlorine electro-activity, *Electrochim. Acta*, 2012, **78**, 188-194.

[6] W. Hu, S. Chen, Q. Xia, $IrO_2$/Nb-$TiO_2$ electrocatalyst for oxygen evolution reaction in acidic medium, *Int. J. Hydrogen Energ.*, 2014, **39**, 6967-6976.

[7] M. S. El-Deab, M. I. Awad, A. M. Mohammad, T. Ohsaka, Enhanced water electrolysis: electrocatalytic generation of oxygen gas at manganese oxide nanorods modified electrodes, *Electrochem. Commun.*, 2007, **9**, 2082-2087.

[8] T. Wu, G. Zhao, Y. Lei, P. Li, Distinctive tin dioxide anode fabricated by pulse electrodeposition: high oxygen evolution potential and efficient electrochemical degradation of fluorobenzene, *J. Phys. Chem. C*, 2011, **115**, 3888.

[9] X. Chen, G. Chen, P.L. Yue, Stable Ti/$IrO_x$-$Sb_2O_5$-$SnO_2$ anode for $O_2$ evolution with low Ir content, *J. Phys. Chem. B*, 2001, **105**, 4623-4628.

[10] Y. Cui, Y. Feng, Z. Liu, Influence of rare earths doping on the structure and electro-catalytic performance of Ti/Sb-$SnO_2$ electrodes, *Electrochim. Acta*, 2009, **54**, 4903-4909.

[11] R. Berenguer, C. Quijada, E. Morallón, Electrochemical characterization of $SnO_2$ electrodes doped with Ru and Pt, *Electrochim. Acta*, 2009, **54**, 5230-5238.

[12] S. Y. Yang, Y. S. Choo, S. Kim, S. K. Lim, J. Lee, H. Park, Boosting the electrocatalytic activities of $SnO_2$ electrodes for remediation of aqueous pollutants by

doping with various metals, *Appl. Catal. B-Environ.*, 2012, **111-112**, 317-325.

[13] Y. Wang, T. Brezesinski, M. Antonietti, B. Smarsly, Ordered mesoporous Sb-, Nb-, and Ta- doped $SnO_2$ thin films with adjustable doping levels and high electrical conductivity, *ACS Nano*, 2009, **3**, 1373-1378.

[14] Y. Chen, L. Hong, H. Xue, W. Han, L. Wang, X. Sun, J. Li, Preparation and characterization of $TiO_2$-NTs/$SnO_2$-Sb electrodes by electrodeposition, *J. Electroanal. Chem.*, 2010, **648**, 119-127.

[15] X. Wu, J. Zhang, Y. Wang, A. Huang, Structure and properties of Ti/TiN/Sb-$SnO_2$ electrodes with plasma sprayed TiN interlayer, *Adv. Mater. Res.*, 2013, **602-604**, 1613-1616.

[16] F. Hu, X. Cui, W. Chen, Pulse Electro-codeposition of Ti/$SnO_2$-$Sb_2O_4$-CNT electrode for phenol oxidation, *Electrochem. Solid ST.*, 2010, **13**, F20-F23.

[17] F. Hu, Z. Dong, X. Cui, W. Chen, Improved $SnO_2$-$Sb_2O_4$ based anode modified with $Cr_3C_2$ and CNT for phenol oxidation, *Electrochim. Acta*, 2011, **56**, 1576-1580.

[18] L. Zhang, L. Xu, J. He, J. Zhang, Preparation of Ti/$SnO_2$-Sb electrodes modified by carbon nanotube for anodic oxidation of dye wastewater and combination with nanofiltration, *Electrochim. Acta*, 2014, **117**, 192-201.

[19] T. Duan, Q. Wen, Y. Chen, Y. Zhou, Y. Duan, Enhancing electrocatalytic performance of Sb-doped $SnO_2$ electrode by compositing nitrogen-doped graphene nanosheets, *J. Hazard. Mater.*, 2014, **280**, 304-314.

[20] T. Duan, Y. Chen, Q. Wen, Y. Duan, Enhanced electrocatalytic activity of nano-TiN composited Ti/Sb-$SnO_2$ electrode fabricated by pulse electrodeposition for

methylene blue decolorization, *RSC Adv.*, 2014, **4**, 57463-57475.

[21] Y. Duan, Q. Wen, Y. Chen, T. Duan, Y. Zhou, Preparation and characterization of TiN-doped Ti/$SnO_2$-Sb electrode by dip coating for orange II decolorization, *Appl. Surf. Sci.*, 2014, **320**, 746-755.

[22] Y. Feng, Y. Cui, B. Logan, Z. Liu, Performance of Gd-doped Ti-based Sb-$SnO_2$ anodes for electrochemical destruction of phenol, *Chemosphere*, 2008, **70**, 1629-1636.

[23] Y. Cui, Y. Feng, J. Liu, N. Ren, Comparison of various organic compounds destruction on rare earths doped Ti/Sb-$SnO_2$ electrodes, *J. Hazard. Mater.*, 2012, **239-240**, 225-232.

[24] H. G. Yang, H. C. Zeng, Self-Construction of Hollow $SnO_2$ Octahedra Based on Two-Dimensional Aggregation of Nanocrystallites, *Angew. Chem.*, 2004, **116**, 6056-6059.

[25] M. I. Mendivil, B. Krishnan, F. A. Sanchez, S. Martinez, J. A. Aguilar-Martinez, G. A. Castillo, D. I. Garcia-Gutierrez, S. Shaji, Synthesis of silver nanoparticles and antimony oxide nanocrystals by pulsed laser ablation in liquid media, *Appl. Phys. A*, 2013, **110**, 809-816.

[26] A. Vantomme, Z.-Y. Yuan, G. Du, B.-L. Su, Surfactant-Assisted Large-Scale Preparation of Crystalline $CeO_2$ Nanorods, *Langmuir* 2005, **21**, 1132-1135.

[27] F. Gu, S. F. Wang, M. K. Lu, G. J. Zhou, D. Xu, D. R. Yuan, Photoluminescence properties of $SnO_2$ nanoparticles synthesized by sol-gel method, *J. Phys. Chem. B*, 2004, **108**, 8119-8123.

[28] S. A. Lajevardi, T. Shahrabi, Effects of pulse electrodeposition parameters on the

properties of Ni-$TiO_2$ nanocomposite coatings, *Appl. Surf. Sci.*, 2010, **256**, 6775-6781.

[29] A. R. Babar, S. S. Shinde, A. V. Moholkar, C. H. Bhosale, J. H. Kim, K. Y. Rajpure, Sensing properties of sprayed antimony doped tin oxide thin films: solution molarity, *J. Alloy. Compd.*, 2011, **509**, 3108-3115.

[30] H. He, H. X. Dai, C. T. Au, Defective structure, oxygen mobility, oxygen storage capacity, and redox properties of RE-based (RE = Ce, Pr) solid solutions, *Catal. Today*, 2004, **90**, 245-254.

[31] C. Terrier, J. P. Chatelon, J. A. Roger, Analysis of antimony doping in tin oxide thin films obtained by the sol-gel Method, *J. Sol-Gel Sci. Techn.*, 1997, **10**, 75-81.

[32] B. Slater, C. R. A. Catlow, D. H. Gay, D. E. Williams, V. Dusastre, Study of surface segregation of antimony on $SnO_2$ surfaces by computer simulation techniques, *J. Phys. Chem. B*, 1999, **103**, 10644-10650.

[33] S. D. Lounis, E. L. Runnerstrom, A. Llordés, D. J. Milliron, Defect chemistry and plasmon physics of colloidal metal oxide nanocrystals, *J. Phys. Chem. Lett.* 2014, **5**, 1564-1574.

[34] N. L. Wu, J. Y. Hwang, P. Y. Liu, C. Y. Han, S. L. Kuo, K. H. Liao, M. H. Lee, S. Y. Wang, Synthesis and Characterization of Sb-Doped $SnO_2$ Xerogel Electrochemical Capacitor, *J. Electrochem. Soc.*, 2001, **148**, A550-A553.

[35] F. Montilla, E. Morallón, A. De Battisti, S. Barison, S. Daolio, J. L. Vázquez, Preparation and characterization of antimony-doped tin dioxide electrodes. part 1. electrochemical characterization, *J. Phys. Chem. B*, 2004, **108**, 5036-5043.

[36] L. K. Xu, J. D. Scantlebury, Electrochemical surface characterization of

$IrO_2$-$Ta_2O_5$ coated titanium electrodes in $Na_2SO_4$ solution, *J. Electrochem. Soc.*, 2003, **150**, B288-B293.

[37] S. Ardizzone, G. Fregonara, S. Trasatti, "Inner" and "outer" active surface of $RuO_2$ electrodes, *Electrochim. Acta*, 1990, **35**, 263-267.

[38] R. Mohammadi, M. Søgaard, T. Ramos, M. Ghassemi, M. B. Mogensen, Electrochemical impedance modeling of a solid oxide fuel cell anode, *Fuel Cells*, 2014, **14**, 645-659.

[39] L. L. Díaz-Flores, R. Ramírez-Bon, A. Mendoza-Galván, E. Prokhorov, J. González-Hernández, Impedance spectroscopy studies on $SnO_2$ films prepared by the sol-gel process, *J. Phys. Chem. Solids*, 2003, **64**, 1037-1042.

[40] A. Ourya, A. Kirchev, Y. Bultel, Oxygen evolution on alpha-lead dioxide electrodes in methanesulfonic acid, *Electrochim. Acta*, 2012, **63**, 28-36.

[41] T. Pajkossy, Impedance of rough capacitive electrodes, *J. Electroanal. Chem.*, 1994, **364**, 111-125.

[42] F. R. Costa, D. V. Franco, L. M. D. Silva, Electrochemical impedance spectroscopy study of the oxygen evolution reaction on a gas-evolving anode composed of lead dioxide microfibers, *Electrochim. Acta*, 2013, **90**, 332-343.

[43] A. Chen, S. Nigro, Influence of a nanoscale gold thin layer on Ti/$SnO_2$-$Sb_2O_5$ electrodes, *J. Phys. Chem. B*, 2003, **107**, 13341-13348.